CHEMISTRY OF MATERIALS
Cite This: Chem. Mater. 2019, 31, 8515−8522
Article
pubs.acs.org/cm

Temperature-Dependent Thermal Decomposition Pathway of Organic−Inorganic Halide Perovskite Materials

Lin Ma,[†] Deqiang Guo,[†] Mengting Li,[‡] Cheng Wang,[†] Zilin Zhou,[†] Xin Zhao,[†] Fangteng Zhang,[†] Zhimin Ao,*[,‡] and Zhaogang Nie*[,†]

[†]School of Physics and Optoelectronic Engineering, and [‡]Guangzhou Key Laboratory of Environmental Catalysis and Pollution Control, Institute of Environmental Health and Pollution Control, School of Environmental Science and Engineering, Guangdong University of Technology, Guangzhou 510006, China

Supporting Information

ABSTRACT: The thermal decomposition products and kinetics of two typical organic−inorganic halide perovskites, $CH_3NH_3PbI_3$ ($MAPbI_3$) and $HC(NH_2)_2PbI_3$ ($FAPbI_3$), were investigated via simultaneous thermogravimetric analysis coupled with Fourier transform infrared spectroscopy. NH_3 and CH_3I were verified as the major thermal decomposition gases of $MAPbI_3$. Furthermore, for the first time, methane (CH_4) was observed as a thermal degradation product of $MAPbI_3$ at elevated temperatures. In contrast to conventional wisdom, $(HCN)_3$ (trimerized HCN) and NH_3 were demonstrated as the major gaseous decomposition products of $FAPbI_3$ at lower temperatures, while HCN and NH_3 became dominant at high temperatures (>360 °C). The hybrid experimental/theoretical results presented in this study will further our understanding of the perovskite decomposition mechanism and provide new insights into designing of long-term stable perovskite-based devices.

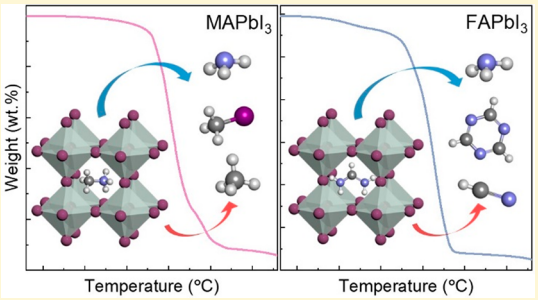

INTRODUCTION

The organic−inorganic halide perovskite (OIHP)-based photovoltaics have achieved unprecedented rises in power conversion efficiency (PCE) in recent years, with the best PCE reaching 25.2%.[1] OIHPs have also been widely exploited in light-emitting diodes (LEDs), lasers, photodetectors, and radiation detectors.[2−5] To date, lead halide perovskites employing organic cations such as methylammonium ($CH_3NH_3^+$), formamidinium ($HC(NH_2)_2^+$), or their mixtures are the most extensively investigated in perovskite-based devices.[6] The two champion OIHPs, methylammonium lead iodide $CH_3NH_3PbI_3$ ($MAPbI_3$) and formamidinium lead iodide $HC(NH_2)_2PbI_3$ ($FAPbI_3$), possess unique merits featuring high absorption coefficients, broad solar spectrum harvesting range, long carrier diffusion lengths, and high charge carrier mobilities.[6−9] However, issues in photo, humidity, and thermal stabilities inhibit them toward large-scale commercialization. The degradation of OIHPs under light and humidity was proven to be related to the escape of organic cations from Pb−I cages, reactions of organic cations with oxygen, or water.[10,11] However, the intrinsic thermal decomposition properties of $MAPbI_3$ and $FAPbI_3$ remain ambiguous. To be more specific, PbI_2 is known as the condensed phase degradation product of $MAPbI_3$. Yet, far less information is available about gas phase products released upon thermal degradation. It is of interest to optimize the synthetic and annealing conditions of OIHP materials, in order to achieve high-performing, reproducible, and stable perovskite-based devices.[12−14]

Traditional thermogravimetric analysis (TGA) experiments provided only total mass loss rates and percentages, with little information on compositions and kinetics of the gaseous species released during thermal decomposition. Different interpretations were proposed in previous literature regarding chemical compositions of gas phase thermal degradation products of $MAPbI_3$. Two proposed pathways for thermal decomposition of $MAPbI_3$ are as follows

$$CH_3NH_3PbI_3 \xrightarrow{\Delta} CH_3NH_2 + HI + PbI_2 \quad (1a)$$

$$CH_3NH_3PbI_3 \xrightarrow{\Delta} NH_3 + CH_3I + PbI_2 \quad (1b)$$

(1) Dualeh et al.[15] proposed that HI and CH_3NH_2 were released consecutively based on the weight loss percentage data from TGA. Later on, Brunetti et al.[16] and Nenon et al.[17] proposed the same decomposition pathway by mass spectrometric studies on $MAPbI_3$ (eq 1a). (2) Williams et al.[18] observed weak NH_3 features by measuring Fourier transform infrared (FTIR) spectra during TGA. They suggested that the decomposition of $MAPbI_3$ is similar to methylammonium iodide (MAI), which decomposes into NH_3 and CH_3I (eq 1b). Juarez-Perez et al.[19] observed a similar decomposition path by employing TGA coupled with mass spectrometry (MS). Latini et al.[14] also performed TGA−MS measurements and predicted

Received: August 7, 2019
Revised: September 20, 2019
Published: September 24, 2019

DOI: 10.1021/acs.chemmater.9b03190
Chem. Mater. 2019, 31, 8515−8522

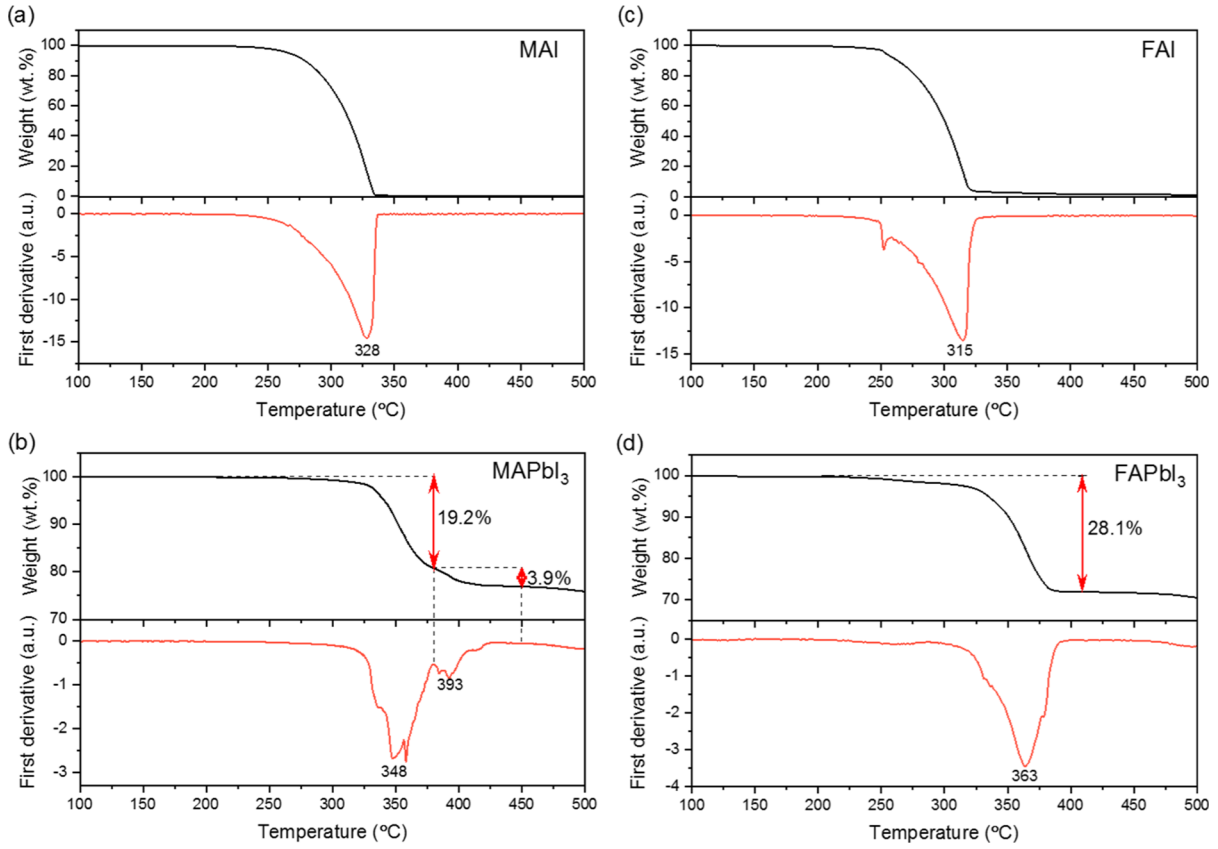

Figure 1. TGA and the first derivative of TGA curves for (a) MAI, (b) $MAPbI_3$, (c) FAI, and (d) $FAPbI_3$ at a heating rate of 5 °C min^{-1} in nitrogen.

that the decomposition path of $MAPbI_3$ might depend on actual operative conditions. McLeod and Liu. also suggested that $MAPbI_3$ can decompose following eqs 1a and 1b under either kinetic or thermodynamic control.[20] $FAPbI_3$ was found to have better thermal stability than $MAPbI_3$ when the film was stored at 150 °C, owing to its stronger interactions of FA cations with PbI_6 octahedra than of MA cations.[9] However, very limited data are available on the thermal decomposition behaviors of $FAPbI_3$. Han et al.[21] measured the TGA of $FAPbI_3$ single crystal and proposed that $FAPbI_3$ thermally decomposed into hydrogen iodide and formamidinium. Recently, Juarez-Perez et al.[22] reported that thermal decomposition of $FAPbI_3$ releases HCN, $(HCN)_3$, and NH_3 as gaseous products via TGA coupled with MS analysis.

In this study, we evaluated thermal decomposition processes of these two representative OIHPs, $MAPbI_3$ and $FAPbI_3$, by correlating TGA with FTIR spectroscopy. Compared to MS measurements, which may cause fragmentations in sample molecules ionized by electron bombardments, FTIR spectra can work as nondestructive fingerprints to identify chemical natures of the evolved gases during thermal decomposition. The decomposition paths of both perovskite materials were found to rely on the temperature. $MAPbI_3$ releases ammonia (NH_3) and methyl iodide (CH_3I) gases at lower temperatures (275−350 °C). Interestingly, additional gaseous product, methane (CH_4), was observed at higher temperatures (above 350 °C). $FAPbI_3$ releases *s*-triazine $(HCN)_3$ and NH_3 at lower temperatures (245−285 °C), while hydrogen cyanide (HCN) and NH_3 were found dominant at elevated temperatures above 360 °C.

RESULTS AND DISCUSSION

The as-prepared $MAPbI_3$ and $FAPbI_3$ powders show good crystallinities as shown by the X-ray diffraction (XRD) patterns (Figure S1, Supporting Information). TGA trace and FTIR spectra of evolved gases were recorded simultaneously during heating of $MAPbI_3$ from room temperature to 800 °C, as shown in Figure S2 (Supporting Information). The FTIR signal mainly concentrates in the temperature range of 250−450 °C. PbI_2 is known as the condensed phase degradation product of $MAPbI_3$ at a temperature above 450 °C. Herein, we only focus on TGA and FTIR data up to 500 °C to evaluate the chemical nature of evolved gaseous decomposition products. For comparison, we also measured thermal decomposition behavior of the organic precursors MAI and formamidinium iodide (FAI). TGA and its first derivative traces of MAI, $MAPbI_3$, FAI, and $FAPbI_3$ powders are presented in Figure 1. As shown in Figure 1a, MAI undergoes 100% weight loss in one single step. In contrast, there are two weight loss events for $MAPbI_3$ (Figure 1b): the first weight loss (19.2%) takes place between 250 and 380 °C; the second weight loss around 4% occurs sequentially till 450 °C, consistent with previously reported TGA traces of $MAPbI_3$.[15,19,23] In comparison to MAI, an apparent temperature delay (around 20 °C) of the weight loss onset for $MAPbI_3$ is indicative of the interaction between organic cations $CH_3NH_2^+$ and surrounding Pb−I cages.[24] The remaining 77% weight percentage at 450 °C is in excellent agreement with the calculated weight percent of PbI_2 in $MAPbI_3$ (74%). This indicates that the remaining products after reaching 450 °C are mainly PbI_2 and $MAPbI_3$ released most organic gaseous

DOI: 10.1021/acs.chemmater.9b03190
Chem. Mater. 2019, 31, 8515−8522

decomposition products within the first two weight loss events before reaching 450 °C. The two weight loss events in $MAPbI_3$ were also reported previously; however, their origins are still disputable. Dualeh et al.[15] and Liu et al.[23] assigned the first weight loss step to the release of HI and the second weight loss to release of CH_3NH_2 gas according to calculated weight percentages. Williams et al.[18] and Juarez-Perez et al.[19] attributed these weight loss events to the release of CH_3I and NH_3 gases by correlating TGA with FTIR or MS results. We will discuss the origin of these two weight loss events in detail together with FTIR spectra of the evolved gases. It shows that the thermal decomposition of $MAPbI_3$ actually involves three gaseous species, NH_3, CH_3I, and CH_4 (vide infra).

As shown in Figure 1c, FAI undergoes 100% weight loss with two weight loss events before reaching 500 °C. In addition to a predominant event with a maximal weight loss rate at 315 °C, one sharp spike was observed at 252 °C in the first derivative of the TGA curve. $FAPbI_3$ experienced 28.1% weight loss (Figure 1d) at around 420 °C, which correlates well with the calculated weight fraction of the organic component (FAI) in $FAPbI_3$ (27.2%). There is also a temperature delay for the thermal decomposition onset in $FAPbI_3$ compared with FAI (Figure 1c,d). The relatively larger temperature delay value (around 50 °C) in $FAPbI_3$ compared with $MAPbI_3$ (around 20 °C) indicates that the interactions between FA cations and inorganic Pb−I matrices are stronger than MA cations in perovskite structures.

In order to identify the chemical nature of gaseous thermal decomposition products, FTIR spectra of the evolved gases were recorded simultaneously during TGA. The obtained FTIR patterns of MAI and $MAPbI_3$ are presented in Figure 2, together with standard IR spectra of three gases, ammonia (NH_3), methyl iodide (CH_3I), and methane (CH_4) from ref 25 As shown in Figure 2a, IR characteristics of NH_3 and CH_3I were detected in the FTIR pattern of MAI, labeled with purple and green stars, respectively. The evolution curves of FTIR intensity versus temperature/time at representative wavenumbers of NH_3 and CH_3I (Figure S3, Supporting Information) show that NH_3 and CH_3I evolved concurrently during MAI decomposition. Although quantum chemistry study predicts that decomposition of primary alkylammonium halides forms CH_3NH_2 and hydrogen halide,[26] the obtained data indicates the thermal decomposition of MAI releases NH_3 and CH_3I, with the reaction path shown in eq 2

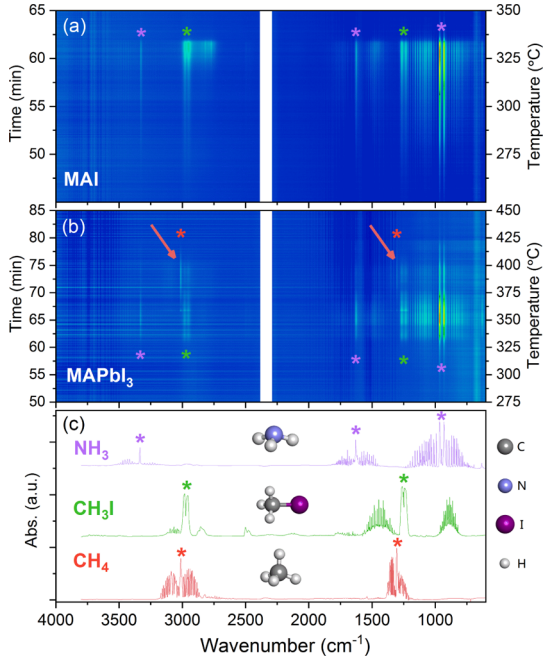

Figure 2. 2D contour plot of the in situ FTIR spectra of evolved gases from (a) MAI and (b) $MAPbI_3$ during TGA. (c) IR reference spectra of NH_3, CH_3I, and CH_4 in the gas phase.[25] The background signals from CO_2 in (a,b) were removed for clarity.

$$CH_3NH_3I \xrightarrow{\Delta} NH_3 + CH_3I \quad (2)$$

As shown in Figure 2b, the FTIR spectral pattern of $MAPbI_3$ at temperature <360 °C is analogous to that of MAI (Figure 2a). It is also worth noting that we did not observe any spectral features corresponding to gaseous CH_3NH_2 (780 and 2961 cm^{-1}) or HI (2229 cm^{-1}).[25,27] The absorption coefficient of CH_3NH_2 (~400 × 10^{-21} cm^2/molecule at 780 cm^{-1}) is comparable to that of NH_3 (~500 × 10^{-21} cm^2/molecule at 966 cm^{-1}) and around 3 order of magnitude larger than that of HI (~0.5 × 10^{-21} cm^2/molecule at 2229 cm^{-1}).[28] Therefore, we can conclude that the decomposition route as depicted in eq 1b is more thermally favored than eq 1a. Therefore, the major gaseous thermal decomposition products of $MAPbI_3$ are NH_3 and CH_3I, rather than CH_3NH_2 and HI proposed via the TGA−MS study.[17] It is worthy to note that the thermal decompositions studied in this work occur at relatively high temperatures, well above perovskite photovoltaic operating temperatures. The decomposition pathways at lower temperatures (<100 °C) could be different. Ciccioli and Latini. suggested that $MAPbI_3$ decomposition to NH_3 and CH_3I is thermodynamically favored at high temperatures while the release of HI and CH_3NH_2 is dominated at low temperatures through thermodynamic analysis based on the available experimental data.[29] First-principles density functional theory (DFT) calculations also suggests that the decomposition pathway involving NH_3 and CH_3I is more favored compared with the one involving CH_3NH_2 and HI in the temperature range of 20−600 °C.[19] At elevated temperatures (>360 °C), additional FTIR features were observed in the FTIR pattern of $MAPbI_3$ (Figure 2b) but absent in MAI as indicated with red stars and arrows in Figure 2b. FTIR spectra of the evolved gases recorded at different temperatures during TGA are also plotted in Figure 3a. Intriguingly, in addition to the NH_3 and CH_3I spectral characteristics, the key IR features of methane CH_4 (1306 and 3016 cm^{-1})[25] were detected at higher temperatures (labeled with red arrows). The evolution of FTIR intensity at representative wavenumbers of NH_3, CH_3I and CH_4 versus temperature during TGA is plotted in Figure 3b. NH_3 and CH_3I evolved concurrently and their evolution curves correspond well to the mirror image of the first derivative of the TGA trace (Figure 1b lower panel). This suggests that NH_3 and CH_3I were released simultaneously from $MAPbI_3$ with the decomposition route as depicted in eq 1b. However, the onset temperature of the CH_4 evolution curve is apparently delayed compared to those of NH_3 and CH_3I. It indicates that, at higher temperatures (>360 °C), in addition to NH_3 and CH_3I, CH_4 was also released during thermal degradation of $MAPbI_3$. To our best knowledge, the flammable CH_4 as a thermal decomposition product of $MAPbI_3$ has never been reported previously. The temperature

DOI: 10.1021/acs.chemmater.9b03190
Chem. Mater. 2019, 31, 8515−8522

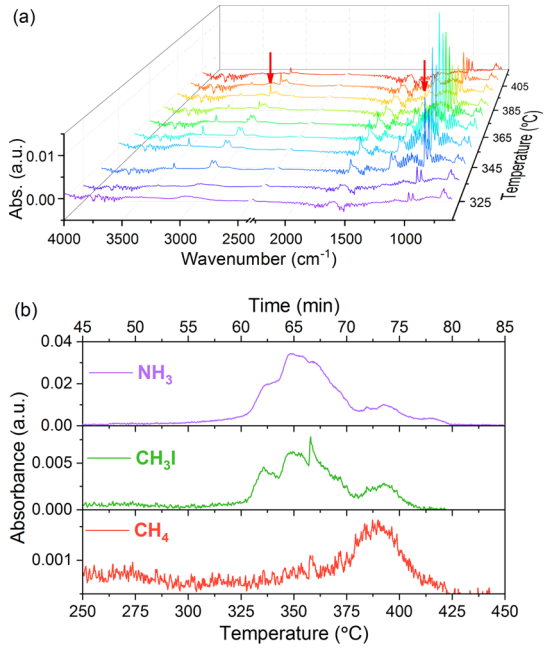

Figure 3. (a) Temperature-dependent FTIR spectra of evolved gases and (b) the evolution of the representative FTIR signal of NH_3 (966 cm^{-1}), CH_3I (1266 cm^{-1}), and CH_4 (3016 cm^{-1}) vs temperature (time) during TGA heating of $MAPbI_3$.

range of CH_4 evolution corresponds well with the second weight loss step in the TGA curve of $MAPbI_3$ (Figure 2b). As mentioned above, this weight loss step was attributed to the release of CH_3NH_2 gas according to the corresponding weight loss percentage.[15,23] Herein, CH_4 fingerprint is clearly seen in the FTIR pattern of $MAPbI_3$ but absent in MAI. This suggests that this decomposition behavior is related to CH_4 formation and occurs only when the MA cation is incorporated into the $MAPbI_3$ perovskite structure.

To explore the origin of methane, we performed isothermal heating experiment of $MAPbI_3$. The temperature was heated from room temperature to 390 °C at a heating rate of 30 °C/min and kept constant for around 30 min. As shown in Figure S4 (Supporting Information), FTIR features of NH_3 and CH_3I decay synchronously due to the weight loss of $MAPbI_3$ thermal decomposition. However, the FTIR feature of CH_4 decays differently: the drop of FTIR intensity with time is less steep and more fluctuated than that of NH_3 or CH_3I. This indicates that the formation of CH_4, NH_3 and CH_3I at high temperatures does not follow a stoichiometric equation. At around 1.5 min, there is a sudden rise and decay in the FTIR trace of CH_4, which is also visible in the CH_3I FTIR trace but absent in the NH_3 FTIR signal. This infers that the CH_4 formation is related to CH_3I rather than NH_3. Considering the bond dissociation energies of $I-CH_3$, $H-CH_2I$, and $H-NH_2$ are 232, 431, and 435 kJ/mol, respectively,[30] the CH_4 formation is most probably due to dissociation of the relatively weak $I-CH_3$ bond to form methyl and iodine radicals which then attract hydrogen radicals to form CH_4 and HI. However, the absorption coefficient of HI (~0.5×10^{-21} cm^2/molecule at 2229 cm^{-1}) is around 3000 times smaller than that of CH_4 (~1500×10^{-21} cm^2/molecule at 3016 cm^{-1}).[28] Therefore, we did not observe the IR spectral signal corresponding to HI. One possible origin of $^{\bullet}H$ is from the homolytic cleavage of methyl groups to form free hydrogen radicals.[31] Another possible origin of $^{\bullet}H$ is from the inevitable water involved during sample preparation or sample transferring to the TGA chamber. If the hydrogen radical is from water, the oxygen element will be expected to remain in the residual powder after thermal heating. Therefore, we measured the X-ray photoelectron spectroscopy (XPS) spectra of the yellow residual powder remained after the $MAPbI_3$ TGA experiment (Supporting Information, Figure S5). However, the detected oxygen signal in the XPS spectra is almost negligible. Therefore, we can rule out the origin of CH_4 due to humidity or oxygen-induced impurities.

FTIR patterns of evolved gases during thermal decomposition of FAI and $FAPbI_3$ are shown in Figure 4. The FTIR

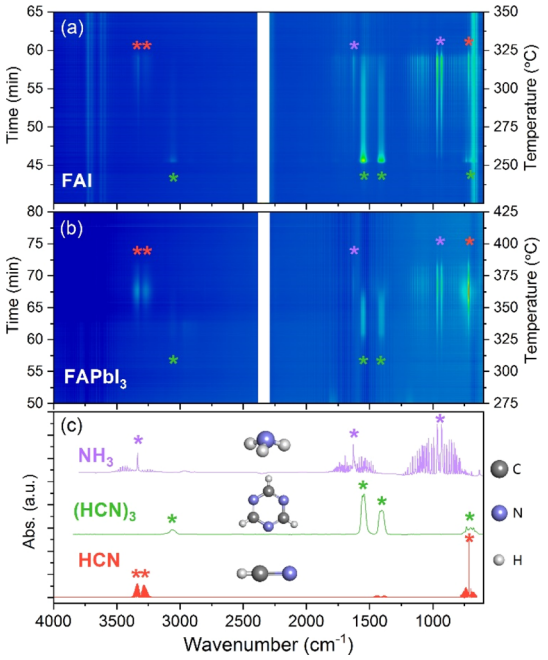

Figure 4. 2D contour plot of the in situ FTIR spectra of evolved gases from (a) FAI and (b) $FAPbI_3$ during TGA. (c) IR reference spectra of NH_3, $(HCN)_3$ (*s*-triazine), and HCN in the gas phase.[25] The background signals from CO_2 in (a,b) were removed for clarity.

pattern of FAI (Figure 4a) is quite different from that of MAI (Figure 2a). Standard IR spectra from ammonia (NH_3), *s*-triazine $(HCN)_3$, and hydrogen cyanide (HCN) are also plotted in Figure 4c for reference. In addition to spectral features of NH_3 (purple stars), pronounced IR characteristics of *s*-triazine $(HCN)_3$ (green stars) and HCN (red stars) were observed in the FTIR pattern of FAI. Previous literature suggests that amidines thermally decompose into NH_3 and corresponding nitriles. The resulting nitriles are often polymerized to yield additional secondary products.[32] Therefore, we expect NH_3 and HCN as the primary decomposition products of FAI, and polymerized $(HCN)_x$ may form as a secondary product. However, the FTIR pattern of FAI (Figure 4a) is dominated by IR features from $(HCN)_3$ and NH_3 in the lower temperature range (245–285 °C). Together with the FTIR evolution curves (Figure S6, Supporting Information), we conclude that the decomposition of FAI releases $(HCN)_3$ and NH_3 at lower temperatures as described by eq 3a. As temperature rises, additional FTIR characteristics corresponding to HCN became observable (labeled with red stars in Figure 4a). Therefore, the decomposition process of FAI at

DOI: 10.1021/acs.chemmater.9b03190
Chem. Mater. 2019, 31, 8515–8522

elevated temperatures can be depicted by eqs 3a and 3b, releasing NH_3, $(HCN)_3$, and HCN as gaseous degradation products.

$$3CH(NH_2)_2I \xrightarrow{\Delta} (HCN)_3 + 3NH_3 + 3HI \quad (3a)$$

$$CH(NH_2)_2I \xrightarrow{\Delta} HCN + NH_3 + HI \quad (3b)$$

Characteristic IR absorption bands of NH_3, $(HCN)_3$, and HCN were also observed in the FTIR pattern of $FAPbI_3$ during thermal heating (Figure 4b), in agreement with the recent report via the TGA–MS study.[22] Intriguingly, we observed a pronounced temperature dependence on the decomposition products. At lower temperatures (300–330 °C), $(HCN)_3$ and NH_3 FTIR bands are pronounced with an unnoticeable HCN spectral feature. This suggests that the decomposition route of $FAPbI_3$ in lower temperature range can be described by eq 4a. The FTIR spectra of evolved gases recorded at different temperatures and FTIR intensity kinetic curves at representative wavenumbers of three gaseous species are presented in Figure 5. In contrast to the sharp rise and drop

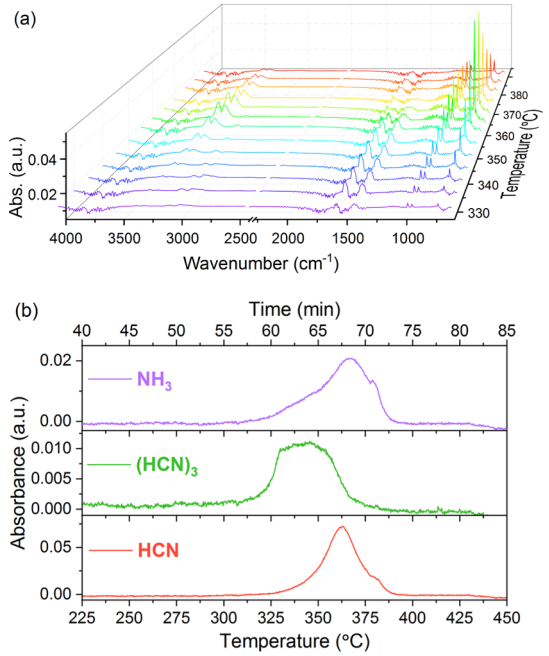

Figure 5. (a) Temperature-dependent FTIR spectra of evolved gases and (b) the evolution of the representative FTIR signal of NH_3 (966 cm^{-1}), $(HCN)_3$ (1546 cm^{-1}), and HCN (712 cm^{-1}) vs temperature (time) during TGA heating of $FAPbI_3$.

in a narrow temperature range 240–260 °C in FAI (Figure S6, Supporting Information), the evolution of $(HCN)_3$ occurs at around 300 °C. It reaches a maximum at around 335 °C, keeping a plateau till 354 °C. Then, it decreases gradually till 400 °C. The decrease of $(HCN)_3$ is accompanied by the formation of HCN. The evolution of HCN reaches a maximum at 363 °C. At higher temperatures, FTIR spectra of evolved gases are dominated by spectral features of HCN and NH_3. Therefore, the decomposition route of $FAPbI_3$ at an elevated temperature can be depicted by eq 4b, releasing HCN and NH_3 as major decomposition products. It is worthy to mention that although HI is proposed as a decomposition product of $FAPbI_3$ or FAI as shown in eqs 3a and 4a, we have not seen any representative IR feature corresponding to HI (ca. 2229 cm^{-1}) in the FTIR patterns. It is probably due to the much lower absorption coefficient of HI compared with NH_3, $(HCN)_3$, or HCN (about 2 order of magnitude lower based on the data from VPL molecular spectroscopic database[28]).

$$3CH(NH_2)_2PbI_3 \xrightarrow{\Delta} (HCN)_3 + 3NH_3 + 3HI + 3PbI_2 \quad (4a)$$

$$CH(NH_2)_2PbI_3 \xrightarrow{\Delta} HCN + NH_3 + HI + PbI_2 \quad (4b)$$

To verify the origin of HCN and the relationship between HCN and $(HCN)_3$ at high temperature, the isothermal heating experiment was implemented for $FAPbI_3$. As shown in Figure 6, the temperature was heated from room temperature to 340

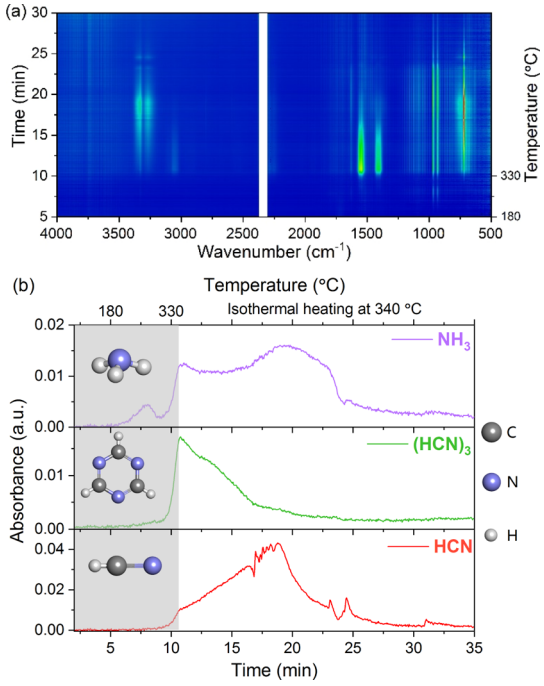

Figure 6. (a) 2D contour plot of in situ FTIR spectra during isothermal heating of $FAPbI_3$ in N_2 at 340 °C (the background signal from CO_2 was removed for clarity). (b) Kinetics of the representative FTIR signal of NH_3 (966 cm^{-1}), $(HCN)_3$ (1546 cm^{-1}), and HCN (712 cm^{-1}) vs time during isothermal heating of $FAPbI_3$. The grey shade indicates the heating process from room temperature to 340 °C.

°C at a heating rate of 30 °C/min and kept constant for around 30 min. As time goes on, the decay of $(HCN)_3$ accompanied by the formation of HCN indicates that HCN might be generated from the decomposition of $(HCN)_3$, in contrast to the conventional wisdom that $(HCN)_3$ is formed via trimerization of HCN as proposed in amidines.[32] We then performed TGA–FTIR measurement on $(HCN)_3$ powder from room temperature to 500 °C (Figure S7, Supporting Information). *s*-Triazine undergoes one single weight loss at very low temperatures (<100 °C). There are no observable HCN spectral features in the FTIR pattern. Previous literature suggests that the triazine ring is stable up to 550 °C.[33] Therefore, it is expected that the *s*-triazine ring is hard to break to form free HCNs. To gain further insight into the pathway of HCN generation, first-principles DFT calculations were conducted. First, direct dissociation pathway $(HCN)_3$ →

DOI: 10.1021/acs.chemmater.9b03190
Chem. Mater. 2019, 31, 8515–8522

3HCN is calculated at different temperatures. The calculated ΔG (Gibbs free enthalpy) evolution in the temperature range of 298.15−1000 K (as shown in Figure S8, Supporting Information) reveals that the reaction is thermodynamically easier (with lower ΔG) as the temperature increases. However, the ΔG at 1000 K is positive with value of 70.8 kcal/mol (it is known that a reaction can go through when $\Delta G < 0$), indicating that the reaction $(HCN)_3 \rightarrow 3HCN$ is not realistic to occur even at high temperatures. The other investigated reaction pathway is that the decomposition of *s*-triazine involves •H attacker. Hydrogen radicals can be generated from HI decomposition or prior to HI formation. All possible attack sites and pathways were taken into consideration as shown in Figure 7. When the first •H attacks the *s*-triazine ring

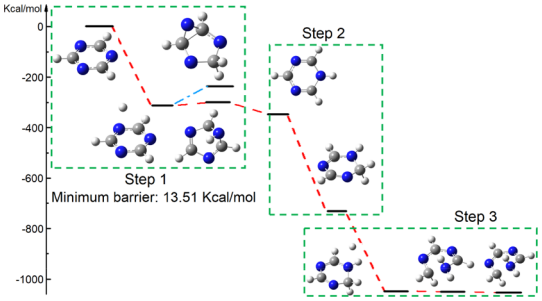

Figure 7. Profile of the potential energy surface for the reaction channel of *s*-triazine with •H. Gray, white, and blue balls represent the carbon, hydrogen, and nitrogen atoms, respectively.

(step 1), the formation of N−H bond with a barrier of 13.51 kcal/mol occurs prior to the C−H bond formation with a barrier of 74.75 kcal/mol. The second •H subsequently binds with C^+ and the $\pi-\pi$ conjugative structure is broken (step 2), resulting in the formation of sp^3 C. The C−N singlet bond can be attacked by subsequent •H with a negative barrier of −3.51 kcal/mol (step 3). Hence, the refractory *s*-triazine ring is broken and the following formation of HCN becomes feasible. The rate-determining step is the first step with the reaction barrier of 13.51 kcal/mol, which can proceed spontaneously at room temperature. It is interesting to note the involvement of hydrogen radicals in the formation of both CH_4 (in $MAPbI_3$) and HCN (in $FAPbI_3$). Further efforts (such as electron paramagnetic resonance spectroscopy) may be helpful to detect the •H and to explore the role of •H in thermal decomposition of perovskites; however, it is beyond the scope of this study here.

CONCLUSIONS

In summary, thermal decomposition processes of OIHPs were elucidated using the TGA−FTIR technique. The thermal decomposition behavior of $MAPbI_3$ and $FAPbI_3$ at the early stage was generally analogous to their organic precursors MAI or FAI, indicating that a meticulous choice of organic cations may further improve the stability of perovskites. We demonstrated that the gaseous decomposition products of OIHPs markedly rely on temperature. At lower temperatures, thermal decomposition of $MAPbI_3$ releases ammonia (NH_3) and methyl iodide (CH_3I) gases. At high temperatures (>350 °C), the decomposition of $MAPbI_3$ also involves a small amount of the methane (CH_4) formation. Thermal degradation of $FAPbI_3$ at lower temperatures releases *s*-triazine $(HCN)_3$ and NH_3. However, HCN and NH_3 were found as the primary decomposition gaseous products of $FAPbI_3$ at temperatures above 360 °C. DFT calculations suggest that the HCN was formed from $(HCN)_3$ via ring opening with hydrogen radical addition. Our observation of flammable methane and toxic hydrogen cyanide formation during thermal decomposition of $MAPbI_3$ and $FAPbI_3$ suggests that additional care should be taken when manipulating a large amount of OIHP materials under high temperature, such as dealing with the recycle of OIHP-based photovoltaics or other devices in future large-scale commercialization. Our study provides a new insight into the thermal stability and degradation mechanism of OIHP materials, and offers beneficial information for further improving the stability of perovskite-based devices.

EXPERIMENTAL METHODS

Materials. Methylammonium iodide (CH_3NH_3I, MAI), formamidinium iodide ($HC(NH_2)_2I$, FAI), and lead iodide (PbI_2) powders were purchased from Xi'an Polymer Light Technology Corp (purity > 99%). The anhydrous dimethylformamide (DMF) was purchased from Sigma-Aldrich. *s*-Triazine powder was purchased from Macklin Inc (purity > 97%). All chemicals were used as received without further purification unless otherwise stated.

Sample Preparation. The $MAPbI_3$ (or $FAPbI_3$) precursor solution was prepared by dissolving 1:1 molar ratio of MAI (or FAI) and PbI_2 in anhydrous DMF, resulting in 35 wt % solution. The precursor solution was deposited onto glass substrates via the doctor-blading method and annealed at 120 °C around 1 h until the film color from yellow turned into dark brown. The obtained perovskite powder was then scratched off the glass substrate carefully and used directly for TGA−FTIR measurements.

Instrumental Analysis. XRD patterns of the $MAPbI_3$ and $FAPbI_3$ powder were collected using a Bruker D8 ADVANCE X-ray diffractometer (Bruker AXS, Germany), with Cu Kα irradiation at 40 kV and 40 mA, and the diffraction angle scan range was 5°−90°. Stepscan mode was used during the XRD analysis with a step size of 0.02 and a dwell time of 0.15 s for each step.

XPS spectra of $MAPbI_3$ and the remaining yellow powder after TGA (PbI_2) were measured by X-ray photoelectron spectroscopy (ESCSLAB 250Xi, Thermo Fisher). All spectra were shifted to account for sample charging using inorganic carbon at 284.80 eV as a reference.

TGA measurements were carried out using a thermal gravimetric analyzer (TG 209 F1, NETZSCH), the simultaneous FTIR spectra of evolved gases were recorded by an FTIR spectrometer (Nicolet iS50, Thermo Fisher). The thermal analysis was performed by placing the sample powder (30 mg $MAPbI_3$ or $FAPbI_3$, 10 mg MAI, FAI or $(HCN)_3$) in an Al_2O_3 crucible, heated from room temperature (26 °C) to 500 °C at a constant rate of 5 °C min^{-1}. N_2 at a flow rate of 60 mL min^{-1} was used as the carrier gas and provided an inert atmosphere. Evolved gases were transferred to the FTIR spectrometer through a 1 m long transfer line heated at 280 °C. The isothermal heating experiments were performed using the same TGA−FTIR setup. The $MAPbI_3$ and $FAPbI_3$ powder were heating from room temperature to 390 and 340 °C, respectively, with a heating rate of 30 °C min^{-1}. The temperature was then kept constant for around 30 min or till the powders ran out. The FTIR spectra of the evolved gases were recorded at the same time.

Computational Methods. First-principles DFT calculations were conducted in Gaussian 09 package.[34] The molecular structure optimization was carried out by B3LYP functional[35,36] combined with 6-311G basis set. The TS method was used to search transitional states, where only one negative eigenvalue was in the diagonalized Hessian matrix. The temperature effect on the reaction was evaluated by free energy change (ΔG), which is determined by the equation: $\Delta G = \Delta H - T\Delta S$, where ΔH is the change in enthalpy, T is the temperature, and ΔS is the change in entropy. It is known that $\Delta H = (\Delta U + P\Delta V)$, $\Delta U = (\Delta E_{tot} + \Delta E_{vib} + \Delta E_{trans} + \Delta E_{rot})$, and $\Delta S = \Delta S_{vib} + \Delta S_{trans} + \Delta S_{rot}$, where ΔU is the change of internal energy, ΔE_{tot} is

DOI: 10.1021/acs.chemmater.9b03190
Chem. Mater. 2019, 31, 8515−8522

the total electronic energy change obtained from DFT calculations, the subscript *vib*, *trans*, and *rot* indicate the components from vibration, translation, and rotation, respectively.

■ ASSOCIATED CONTENT

Supporting Information

The Supporting Information is available free of charge on the ACS Publications website at DOI: 10.1021/acs.chemmater.9b03190.

XRD patterns, TGA data for $MAPbI_3$ till 800 °C, FTIR signal evolution curves of MAI and FAI, FTIR spectra during isothermal heating of $MAPbI_3$, XPS spectra of the residual powder after $MAPbI_3$ TGA, TGA curve, and FTIR pattern of $(HCN)_3$ powder, and the ΔG evolution of *s*-triazine versus temperature (PDF)

■ AUTHOR INFORMATION

Corresponding Authors

*E-mail: zhimin.ao@gdut.edu.cn (Z.A.).
*E-mail: zgnie@gdut.edu.cn (Z.N.).

ORCID

Lin Ma: 0000-0002-1815-6201
Zhimin Ao: 0000-0003-0333-3727

Notes

The authors declare no competing financial interest.

■ ACKNOWLEDGMENTS

We would like to thank Chunxiao Yang from GDUT Analysis and Test Center for the help with TGA experiments. This work was supported by the National Natural Science Foundation of China (11704079, 11874125, 11774071, 21607029 and 21777033), and the Science and Technology Program of Guangzhou (201804010451 and 201904010104).

■ REFERENCES

(1) NREL Efficiency Chart. This plot is courtesy of the National Renewable Energy Laboratory, Golden, CO. Available online: https://www.nrel.gov/pv/assets/pdfs/best-research-cell-efficiencies.20190802.pdf (accessed on Aug 07, 2019).

(2) Cho, H.; Jeong, S.-H.; Park, M.-H.; Kim, Y.-H.; Wolf, C.; Lee, C.-L.; Heo, J. H.; Sadhanala, A.; Myoung, N.; Yoo, S.; Im, S. H.; Friend, R. H.; Lee, T.-W. Overcoming the Electroluminescence Efficiency Limitations of Perovskite Light-Emitting Diodes. *Science* **2015**, *350*, 1222−1225.

(3) Xing, G.; Mathews, N.; Lim, S. S.; Yantara, N.; Liu, X.; Sabba, D.; Grätzel, M.; Mhaisalkar, S.; Sum, T. C. Low-Temperature Solution-Processed Wavelength-Tunable Perovskites for Lasing. *Nat. Mater.* **2014**, *13*, 476−480.

(4) Spina, M.; Lehmann, M.; Náfrádi, B.; Bernard, L.; Bonvin, E.; Gaál, R.; Magrez, A.; Forró, L.; Horváth, E. Microengineered $CH_3NH_3PbI_3$ Nanowire/Graphene Phototransistor for Low-Intensity Light Detection at Room Temperature. *Small* **2015**, *11*, 4824−4828.

(5) Yakunin, S.; Dirin, D. N.; Shynkarenko, Y.; Morad, V.; Cherniukh, I.; Nazarenko, O.; Kreil, D.; Nauser, T.; Kovalenko, M. V. Detection of Gamma Photons Using Solution-Grown Single Crystals of Hybrid Lead Halide Perovskites. *Nat. Photonics* **2016**, *10*, 585.

(6) Grätzel, M. The Light and Shade of Perovskite Solar Cells. *Nat. Mater.* **2014**, *13*, 838−842.

(7) Stranks, S. D.; Eperon, G. E.; Grancini, G.; Menelaou, C.; Alcocer, M. J. P.; Leijtens, T.; Herz, L. M.; Petrozza, A.; Snaith, H. J. Electron-Hole Diffusion Lengths Exceeding 1 Micrometer in an Organometal Trihalide Perovskite Absorber. *Science* **2013**, *342*, 341−344.

(8) Xing, G.; Mathews, N.; Sun, S.; Lim, S. S.; Lam, Y. M.; Gratzel, M.; Mhaisalkar, S.; Sum, T. C. Long-Range Balanced Electron- and Hole-Transport Lengths in Organic-Inorganic $CH_3NH_3PbI_3$. *Science* **2013**, *342*, 344−347.

(9) Eperon, G. E.; Stranks, S. D.; Menelaou, C.; Johnston, M. B.; Herz, L. M.; Snaith, H. J. Formamidinium Lead Trihalide: A Broadly Tunable Perovskite for Efficient Planar Heterojunction Solar Cells. *Energy Environ. Sci.* **2014**, *7*, 982−988.

(10) Misra, R. K.; Aharon, S.; Li, B.; Mogilyansky, D.; Visoly-Fisher, I.; Etgar, L.; Katz, E. A. Temperature- and Component-Dependent Degradation of Perovskite Photovoltaic Materials under Concentrated Sunlight. *J. Phys. Chem. Lett.* **2015**, *6*, 326−330.

(11) Yang, J.; Siempelkamp, B. D.; Liu, D.; Kelly, T. L. Investigation of $CH_3NH_3PbI_3$ Degradation Rates and Mechanisms in Controlled Humidity Environments Using in Situ Techniques. *ACS Nano* **2015**, *9*, 1955−1963.

(12) Song, Z.; Watthage, S. C.; Phillips, A. B.; Tompkins, B. L.; Ellingson, R. J.; Heben, M. J. Impact of Processing Temperature and Composition on the Formation of Methylammonium Lead Iodide Perovskites. *Chem. Mater.* **2015**, *27*, 4612−4619.

(13) Conings, B.; Drijkoningen, J.; Gauquelin, N.; Babayigit, A.; D'Haen, J.; D'Olieslaeger, L.; Ethirajan, A.; Verbeeck, J.; Manca, J.; Mosconi, E.; Angelis, F. D.; Boyen, H.-G. Intrinsic Thermal Instability of Methylammonium Lead Trihalide Perovskite. *Adv. Energy Mater.* **2015**, *5*, 1500477.

(14) Latini, A.; Gigli, G.; Ciccioli, A. A Study on the Nature of the Thermal Decomposition of Methylammonium Lead Iodide Perovskite, $CH_3NH_3PbI_3$: An Attempt to Rationalise Contradictory Experimental Results. *Sustainable Energy Fuels* **2017**, *1*, 1351−1357.

(15) Dualeh, A.; Gao, P.; Seok, S. I.; Nazeeruddin, M. K.; Grätzel, M. Thermal Behavior of Methylammonium Lead-Trihalide Perovskite Photovoltaic Light Harvesters. *Chem. Mater.* **2014**, *26*, 6160−6164.

(16) Brunetti, B.; Cavallo, C.; Ciccioli, A.; Gigli, G.; Latini, A. On the Thermal and Thermodynamic (In)Stability of Methylammonium Lead Halide Perovskites. *Sci. Rep.* **2016**, *6*, 31896.

(17) Nenon, D. P.; Christians, J. A.; Wheeler, L. M.; Blackburn, J. L.; Sanehira, E. M.; Dou, B.; Olsen, M. L.; Zhu, K.; Berry, J. J.; Luther, J. M. Structural and Chemical Evolution of Methylammonium Lead Halide Perovskites During Thermal Processing from Solution. *Energy Environ. Sci.* **2016**, *9*, 2072−2082.

(18) Williams, A. E.; Holliman, P. J.; Carnie, M. J.; Davies, M. L.; Worsley, D. A.; Watson, T. M. Perovskite Processing for Photovoltaics: A Spectro-Thermal Evaluation. *J. Mater. Chem. A* **2014**, *2*, 19338−19346.

(19) Juarez-Perez, E. J.; Hawash, Z.; Raga, S. R.; Ono, L. K.; Qi, Y. Thermal Degradation of $CH_3NH_3PbI_3$ Perovskite into NH_3 and CH_3I Gases Observed by Coupled Thermogravimetry−Mass Spectrometry Analysis. *Energy Environ. Sci.* **2016**, *9*, 3406−3410.

(20) McLeod, J. A.; Liu, L. Prospects for Mitigating Intrinsic Organic Decomposition in Methylammonium Lead Triiodide Perovskite. *J. Phys. Chem. Lett.* **2018**, *9*, 2411−2417.

(21) Han, Q.; Bae, S.-H.; Sun, P.; Hsieh, Y.-T.; Yang, Y.; Rim, Y. S.; Zhao, H.; Chen, Q.; Shi, W.; Li, G.; Yang, Y. Single Crystal Formamidinium Lead Iodide ($FAPbI_3$): Insight into the Structural, Optical, and Electrical Properties. *Adv. Mater.* **2016**, *28*, 2253−2258.

(22) Juarez-Perez, E. J.; Ono, L. K.; Qi, Y. Thermal Degradation of Formamidinium Based Lead Halide Perovskites into Sym-Triazine and Hydrogen Cyanide Observed by Coupled Thermogravimetry-Mass Spectrometry Analysis. *J. Mater. Chem. A* **2019**, *7*, 16912−16919.

(23) Liu, Y.; Yang, Z.; Cui, D.; Ren, X.; Sun, J.; Liu, X.; Zhang, J.; Wei, Q.; Fan, H.; Yu, F.; Zhang, X.; Zhao, C.; Liu, S. F. Two-Inch-Sized Perovskite $CH_3NH_3PbX_3$ (X = Cl, Br, I) Crystals: Growth and Characterization. *Adv. Mater.* **2015**, *27*, 5176−5183.

(24) Glaser, T.; Müller, C.; Sendner, M.; Krekeler, C.; Semonin, O. E.; Hull, T. D.; Yaffe, O.; Owen, J. S.; Kowalsky, W.; Pucci, A.; Lovrinčić, R. Infrared Spectroscopic Study of Vibrational Modes in Methylammonium Lead Halide Perovskites. *J. Phys. Chem. Lett.* **2015**, *6*, 2913−2918.

DOI: 10.1021/acs.chemmater.9b03190
Chem. Mater. 2019, 31, 8515−8522

(25) *NIST Chemistry WebBook, NIST Standard Reference Database Number 69*; Linstrom, P. J., Mallard, W. G., Eds., Evaluated Infrared Reference Spectra; National Institute of Standards and Technology: Gaithersburg MD, 20899, 2009.
(26) Sawicka, M.; Storoniak, P.; Skurski, P.; Błażejowski, J.; Rak, J. TG-FTIR, DSC and Quantum Chemical Studies of the Thermal Decomposition of Quaternary Methylammonium Halides. *Chem. Phys.* **2006**, *324*, 425−437.
(27) Wang, B.; Young Wong, K.; Xiao, X.; Chen, T. Elucidating the Reaction Pathways in the Synthesis of Organolead Trihalide Perovskite for High-Performance Solar Cells. *Sci. Rep.* **2015**, *5*, 10557.
(28) VPL Molecular Spectroscopic Database, http://vpl.astro.washington.edu/spectra/allmoleculeslist08.htm (accessed on Sep 20, 2019).
(29) Ciccioli, A.; Latini, A. Thermodynamics and the Intrinsic Stability of Lead Halide Perovskites $CH_3NH_3PbX_3$. *J. Phys. Chem. Lett.* **2018**, *9*, 3756−3765.
(30) Dean, J. A. *Lange's Handbook of Chemistry*, 15th ed.; McGraw-Hill Inc, 1999.
(31) Carangelo, R. M.; Solomon, P. R.; Gerson, D. J. Application of TG-FT-i.r. to study hydrocarbon structure and kinetics. *Fuel* **1987**, *66*, 960−967.
(32) Shriner, R. L.; Neumann, F. W. The Chemistry of the Amidines. *Chem. Rev.* **1944**, *35*, 351−425.
(33) Oxley, J. C.; Smith, J. L.; Moran, J. S. Decomposition of Azo- and Hydrazo-Linked Bis Triazines. *J. Energ. Mater.* **2009**, *27*, 63−93.
(34) Frisch, M. J.; Trucks, G. W.; Schlegel, H. B.; Scuseria, G. E.; Robb, M. A.; Cheeseman, J. R.; Scalmani, G.; Barone, V.; Mennucci, B.; Petersson, G. A.; Nakatsuji, H.; Caricato, M.; Li, X.; Hratchian, H. P.; Izmaylov, A. F.; Bloino, J.; Zheng, G.; Sonnenberg, J. L.; Hada, M.; Ehara, M.; Toyota, K.; Fukuda, R.; Hasegawa, J.; Ishida, M.; Nakajima, T.; Honda, Y.; Kitao, O.; Nakai, H.; Vreven, T.; Montgomery, J. A., Jr; Peralta, J. E.; Ogliaro, F.; Bearpark, M.; Heyd, J. J.; Brothers, E.; Kudin, K. N.; Staroverov, V. N.; Keith, T.; Kobayashi, R.; Normand, J.; Raghavachari, K.; Rendell, A.; Burant, J. C.; Iyengar, S. S.; Tomasi, J.; Cossi, M.; Rega, N.; Millam, J. M.; Klene, M.; Knox, J. E.; Cross, J. B.; Bakken, V.; Adamo, C.; Jaramillo, J.; Gomperts, R.; Stratmann, R. E.; Yazyev, O.; Austin, A. J.; Cammi, R.; Pomelli, C.; Ochterski, J. W.; Martin, R. L.; Morokuma, K.; Zakrzewski, V. G.; Voth, G. A.; Salvador, P.; Dannenberg, J. J.; Dapprich, S.; Daniels, A. D.; Farkas, O.; Foresman, J. B.; Ortiz, J. V.; Cioslowski, J.; Fox, D. J. *Gaussian 09*. Revision C01.; Gaussian Inc.: Wallingford, 2010.
(35) Becke, A. D. Density-functional thermochemistry. III. The role of exact exchange. *J. Chem. Phys.* **1993**, *98*, 5648−5652.
(36) Lee, C.; Yang, W.; Parr, R. G. Development of the Colle-Salvetti Correlation-Energy Formula into a Functional of the Electron Density. *Phys. Rev. B* **1988**, *37*, 785−789.

DOI: 10.1021/acs.chemmater.9b03190
Chem. Mater. 2019, 31, 8515−8522